JACS
JOURNAL OF THE AMERICAN CHEMICAL SOCIETY
pubs.acs.org/JACS
Article

Fast Surface Oxygen Release Kinetics Accelerate Nanoparticle Exsolution in Perovskite Oxides

Jiayue Wang, Dmitri Kalaev, Jing Yang, Iradwikanari Waluyo, Adrian Hunt, Jerzy T. Sadowski, Harry L. Tuller, and Bilge Yildiz*

Cite This: https://doi.org/10.1021/jacs.2c10256
Read Online

ABSTRACT: Exsolution is a recent advancement for fabricating oxide-supported metal nanoparticle catalysts via phase precipitation out of a host oxide. A fundamental understanding and control of the exsolution kinetics are needed to engineer exsolved nanoparticles to obtain higher catalytic activity toward clean energy and fuel conversion. Since oxygen release via oxygen vacancy formation in the host oxide is behind oxide reduction and metal exsolution, we hypothesize that the kinetics of metal exsolution should depend on the kinetics of oxygen release, in addition to the kinetics of metal cation diffusion. Here, we probe the surface exsolution kinetics both experimentally and theoretically using thin-film perovskite $SrTi_{0.65}Fe_{0.35}O_3$ (STF) as a model system. We quantitatively demonstrated that in this system the surface oxygen release governs the metal nanoparticle exsolution kinetics. As a result, by increasing the oxygen release rate in STF, either by reducing the sample thickness or by increasing the surface reactivity, one can effectively accelerate the Fe^0 exsolution kinetics. Fast oxygen release kinetics in STF not only shortened the prereduction time prior to the exsolution onset, but also increased the total quantity of exsolved Fe^0 over time, which agrees well with the predictions from our analytical kinetic modeling. The consistency between the results obtained from in situ experiments and analytical modeling provides a predictive capability for tailoring exsolution, and highlights the importance of engineering host oxide surface oxygen release kinetics in designing exsolved nanocatalysts.

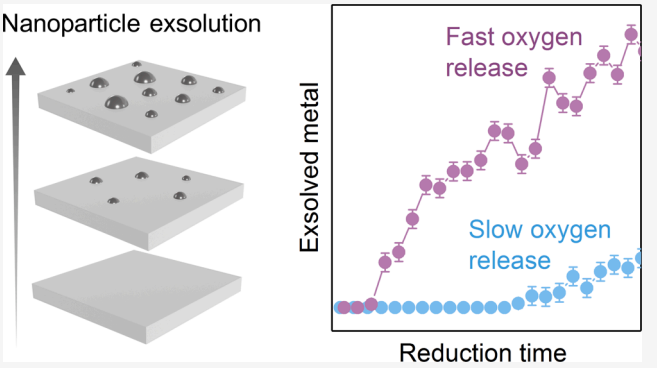

INTRODUCTION

Phase precipitation at the surfaces and interfaces of transition-metal oxides is ubiquitous in clean energy conversion and storage techniques. Many phase precipitation phenomena are undesirable as they can lead to a degradation of the performance of materials, such as Sr segregation in solid oxide fuel cells[1,2] and the segregation of transition-metal ions in lithium-ion batteries.[3,4] Nevertheless, a particular class of cation precipitation, termed "exsolution",[5] has been found to be beneficial, and has been considered as a promising approach to fabricate oxide-supported metal nanocatalysts. In exsolution, the metal cations precipitate out of the host oxides as well-dispersed metal nanoparticles via a single reduction[6−9] or oxidation[10,11] step. Compared to conventional chemical or physical deposition methods,[7,12] the exsolved nanoparticles often exhibit much higher thermal and chemical stabilities as they are highly oriented[13] and are "socketed" into the host oxide.[14−16] Intriguingly, the exsolved nanoparticles may dissolve and regenerate upon redox cycling,[7,17,18] which further increases their lifetimes as catalysts.

While exsolution is powering a revolution in nanoengineering, the underlying reactions controlling it remain poorly understood. To date, the mechanistic understanding of exsolution is mostly gained from equilibrium thermodynamics, with key parameters such as cation segregation energies[19,20] and point defect formation energies.[21,22] Although these thermodynamic descriptors can provide valuable insights, they fail to capture the kinetic processes in exsolution, such as cation diffusion[14,18] and nanoparticle nucleation.[15,21,23,24] On the other hand, a fundamental understanding of the exsolution kinetics is crucial to realize judicious control over particle size and density,[25] and hence the materials' catalytic activities.[26] To bridge this gap, Jo et al.[27] and Neagu et al.[15] have used in situ transmission electron microscopy (TEM) to study the growth kinetics of individual particles during exsolution. Gao et al. analytically modeled the exsolution kinetics under different rate-limiting factors.[28] Recently, Jiang

Received: September 26, 2022

et al. developed a phase-field framework to link the thermodynamic descriptors to the kinetics and microstructure evolution in exsolution.[29] Despite these advances, it remains challenging to understand and control the exsolution kinetics in host oxides.

The global exsolution reaction (Figure 1a), triggered by H_2 reduction, is described using eq 1:

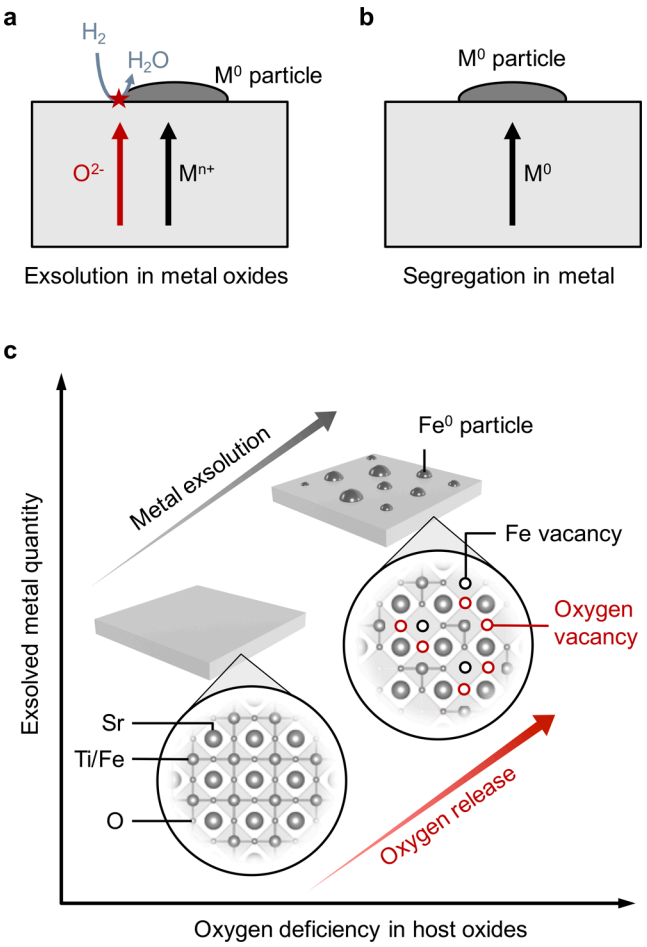

Figure 1. Nanoparticle exsolution and its coupling to the oxygen release process in host oxides. Schematics of (a) nanoparticle exsolution in metal oxides and (b) metal segregation in alloys. Note that while metal segregation in alloy only involves the migration of metallic species (M^0), exsolution in metal oxides involves the migration of both oxygen anions (O^{2-}) and metal cations (M^{n+}), together with surface reactions. (c) Simplified sketch of the coupling between the oxygen deficiency in STF and the total amount of exsolved Fe^0. Fe^0 exsolution makes the material a two-phase system (i.e., metal and perovskites oxides), forming Fe vacancies together with oxygen vacancies in STF. As a result, the total amount of exsolved Fe^0 on the STF surface should be dictated by the degree of oxygen deficiency in STF. In this work, we show that we can effectively tailor the kinetics of Fe^0 exsolution by controlling the oxygen release process in STF.

$$2M^{n+} + nO^{2-} + nH_2 \rightarrow 2V_M^{n-} + nV_O^{2+} + 2M^0 + nH_2O \quad (1)$$

where M^{n+} and M^0 denote the to-be-exsolved metal cations (with the valence state of n) in the host oxides and the exsolved metallic species, respectively. Meanwhile, V_M^{n-} and V_O^{2+} represent the exsolution-induced cation and anion vacancies in the host oxide lattice.[21] As can be seen from eq 1, in addition to metal cations, oxygen anions are also explicitly involved in metal exsolution. In particular, the exsolution process involves the reduction of host oxides (i.e., formation of V_O^{2+}). The kinetics of oxide reduction then depends on the rates of the oxygen release reaction at the surface and the diffusion of oxygen anions within the bulk (Figure 1a). The participation of oxygen in exsolution makes it fundamentally different from the surface segregation process in metal alloys,[30] where metal atoms (M^0) are the only migrating species and no redox reactions take place (Figure 1b). As a result, to exsolve more metal nanoparticles, the host oxides are required to release more oxygen, which results in higher oxygen deficiency (Figure 1c). Motivated by the coupling between the metal exsolution and the oxygen release in host oxides, we hypothesize that we can accelerate the kinetics of metal exsolution by increasing the surface oxygen release kinetics in host oxides.

To examine this hypothesis, we chose single-crystalline thin-film $SrTi_{0.65}Fe_{0.35}O_3$ (STF) as a model system. Previous studies have shown that STF is a promising electrode material in solid oxide fuel cells and electrolysis cells[31−33] that can exsolve metallic iron (Fe^0) nanoparticles[34] as catalysts to enhance water splitting kinetics.[35] In this study, we begin by presenting an analytical kinetic model, which shows that the oxygen release kinetics in thin-film STF are dependent on both the film thickness and surface reactivity. On the other hand, the cation diffusion rate in STF is independent of these two parameters. Therefore, if the exsolution kinetics are limited by surface oxygen release (i.e., surface-limited), they should exhibit a strong dependence on both sample thickness and surface reactivity. Based on these modeling results, we systematically changed the thickness and surface reactivity (by controlling the surface orientation[36,37]) of STF thin films, and experimentally examined their influence on the kinetics of Fe^0 exsolution.

In particular, we employed time-resolved near ambient pressure X-ray photoelectron spectroscopy (NAP-XPS) to probe the Fe^0 exsolution kinetics on STF surface. While previous TEM studies revealed the exsolution kinetics of individual nanoparticles,[15,27] NAP-XPS can provide a unique platform to uncover the statistical exsolution behaviors of a large number of nanoparticles. With the typical X-ray beam size[38] (>1500 μm^2) and surface particle density[21,34] (>10^{10} cm^{-2}), we can simultaneously probe the average exsolution behaviors of more than 10^6 nanoparticles, which yields better statistics. Moreover, while previous TEM studies were limited to polycrystalline samples,[15,27] NAP-XPS can be used to investigate exsolution on single-crystalline samples with well-controlled thickness and orientation, which are essential to quantitatively examine the role of oxygen release kinetics in exsolution. Due to the aforementioned unique advantages, NAP-XPS has gained increasing interest in the field of metal exsolution and has been employed in several studies to investigate the exsolution mechanisms.[21,34,35,39−41] A common practice to date is to use NAP-XPS to probe exsolution while varying the sample temperatures[21,34,39] or electrochemical biases.[35,40] However, such an experimental protocol cannot be used to investigate the kinetic aspects of exsolution as the thermodynamic driving forces for exsolution kept changing during the course of those experiments.[21,34,35,39,40] To bridge this gap, here we develop a novel experimental method for in situ probing materials' exsolution kinetics under a constant reduction condition using time-resolved NAP-XPS. As will be

https://doi.org/10.1021/jacs.2c10256
J. Am. Chem. Soc. XXXX, XXX, XXX−XXX

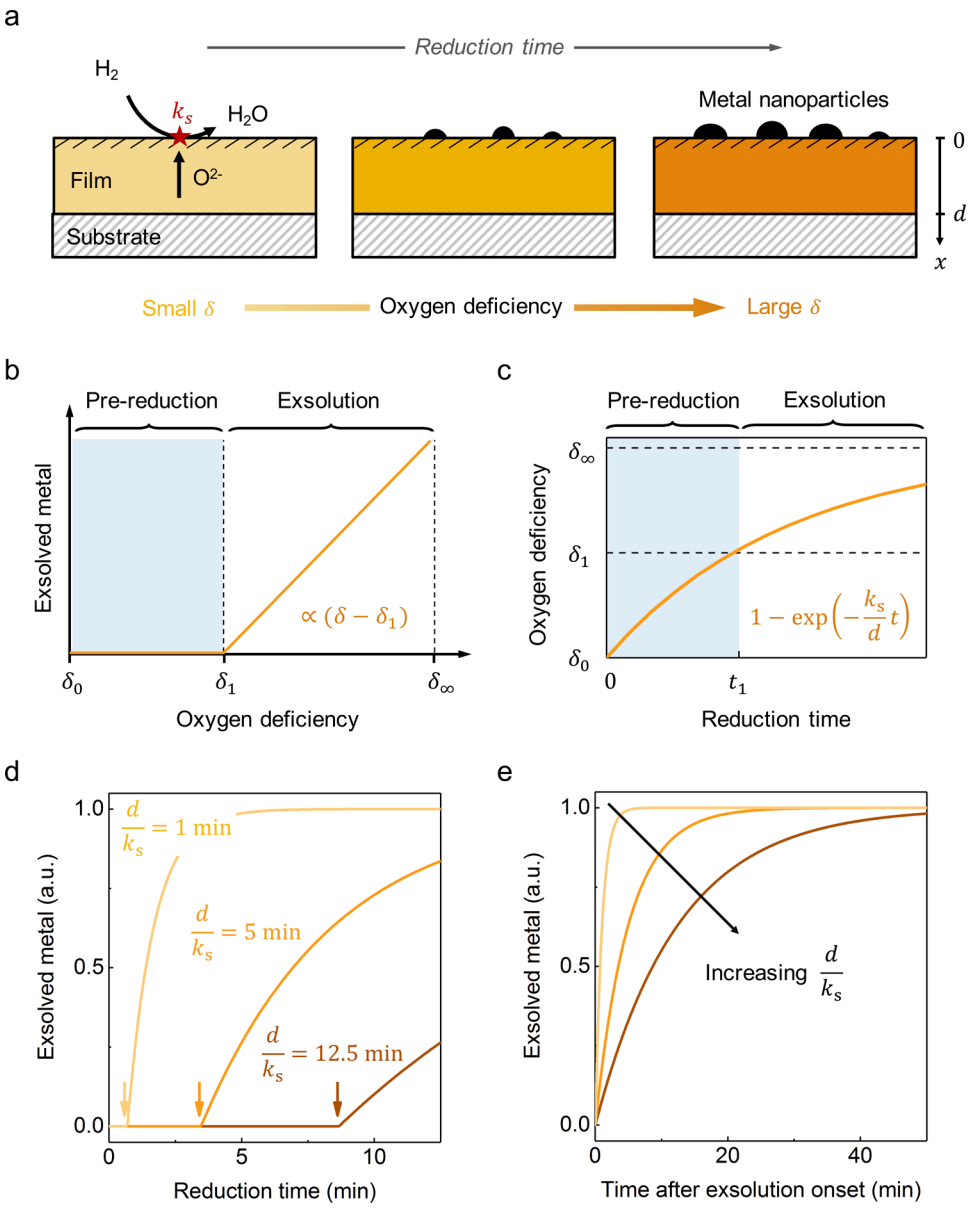

Figure 2. Modeling exsolution kinetics in thin-film samples. (a) Schematic of the surface-limited metal exsolution (with rate constant k_s) on thin-film samples with thickness d. Oxygen deficiency is assumed to be uniform across the sample due to the small thickness. (b) Proposed relationship between the exsolved metal quantity and the oxygen deficiency in the thin-film sample. (c) Calculated oxygen deficiency evolution as a function of reduction time. (d) Calculated prereduction kinetics at different d/k_s values, where the exsolution onsets are marked with arrows. Note that larger d/k_s values postpone the exsolution onset. (e) Calculated exsolution kinetics as a function of d/k_s, where increased d/k_s values result in sluggish metal exsolution. The color coding in Figure 2e is the same as Figure 2d. As illustrated, the kinetic modeling indicates that increasing the surface reactivity (i.e., increase in k_s) and/or reducing the sample thickness (i.e., decrease in d) can accelerate exsolution.

elaborated below, this unique experimental approach can not only quantify the concentration of exsolved metallic species as a function of reduction time, but also reveal the prereduction time required to onset metal exsolution with great precision.

As a result, we demonstrated unequivocally that reducing the sample thickness and increasing the surface reactivity have similar effects in accelerating the Fe^0 exsolution kinetics in STF surface, which agree well with the surface-limited exsolution kinetics derived from our analytical modeling. These findings suggest that the surface oxygen release process is rate-liming for Fe^0 exsolution in STF, so that increasing the oxygen release rate can be an effective approach to boost Fe^0 exsolution in STF. The results presented in this work provide fundamental understanding of metal nanoparticle exsolution kinetics and new kinetics-based directions for engineering exsolved nanocatalysts to boost their catalytic activities toward clean energy and fuel conversion.

THEORY

To elucidate our hypothesis behind the experimental design, in this section, we present analytical models for the Fe^0 exsolution kinetics on the surface of thin-film STF. In particular, we discuss two extreme cases where the exsolution kinetics is either controlled by the surface oxygen release process (i.e., surface-limited) or by the cation diffusion process (i.e., cation diffusion-limited) in host oxides. As a result, we show that if the exsolution kinetics are surface-limited, they will be greatly affected by both the film thickness and the surface reactivity.

https://doi.org/10.1021/jacs.2c10256
J. Am. Chem. Soc. XXXX, XXX, XXX−XXX

On the other hand, if the exsolution kinetics are limited by cation diffusion, they would be insensitive to the two factors described above. We do not discuss the case where exsolution is limited by oxygen diffusion because, in general, oxygen diffusion[42] is much faster than that of metal cations[43] in perovskite oxides. Moreover, for thin films (as in our case), oxygen diffusion is often not rate-limiting for oxide reduction.[44,45]

Surface-Limited Exsolution Kinetics. As shown in Figure 2a, the modeled thin-film geometry has an infinite width, but a thickness of d along the direction, x, of mass transport. Here, $x = 0$ represents the STF surface. Thermodynamically, we define the relationship between the surface oxygen deficiency ($\delta(x = 0)$) and the total quantity of exsolved metal (I) on the STF surface as follows:

$$I = \begin{cases} 0, \ \delta_0 \le \delta(x = 0) < \delta_1 \\ c \times d^* \times (\delta(x = 0) - \delta_1), \ \delta_1 \le \delta(x = 0) < \delta_\infty \end{cases} \tag{2}$$

where δ_0 and δ_∞ represent the surface oxygen deficiency of the as-prepared oxidized sample and the sample that completes the exsolution process, respectively. δ_1 denotes the critical surface oxygen deficiency at the metal exsolution onset. Meanwhile, d^* is the thickness of the near-surface region in STF that acts as the metal reservoir during surface exsolution. In the modeling, we set $d^* = 2$ nm. This is because we have recently shown that the Fe atoms in the surface exsolved Fe^0 nanoparticles on STF are mainly extracted from a very thin layer (~2 nm) near the STF surface, while the bulk of the STF film was not affected.[34] Finally, c is a constant coefficient that accounts for the stoichiometric relationship between the metal cations and oxygen anions.

As schematically shown in Figure 2b, eq 2 depicts a two-step exsolution process, which has been described in more detail in our previous study.[21] During the first step (i.e., prereduction, highlighted in blue in Figure 2b,c), the host oxide continues to release oxygen, while remaining single-phase, until it reaches the critical oxygen deficiency for exsolution (δ_1). Then, upon further reduction, metal exsolution begins when $\delta(x = 0) > \delta_1$, making the material a two-phase system (metal + metal oxides). In this model, we assume that the total exsolved metal intensity (I) is linearly proportional to the excess oxygen deficiency ($\delta(x = 0) - \delta_1$) in the host oxide. The linear relationship is reasonable, because during the second step, the ratio between the quantities of the released oxygen and precipitated metal should be linearly constrained by charge neutrality (see eq 1), resembling Schottky defect[21] formation in oxides (Figure 1c).

Having established the relationship between the surface oxygen deficiency $\delta(x = 0)$ and the total exsolved metal quantity I on the STF surface (i.e., the thermodynamics), we now discuss how $\delta(x = 0)$ and I evolve as a function of reduction time (i.e., the kinetics). For this purpose, we model the transient reduction response of thin-film samples to a step-change in the sample surroundings. The step-change is set to be introduced at $t = 0$, which initiates the sample reduction. For simplicity, we assume that the kinetics of surface oxygen release reactions are first order in concentration, so that we can express the surface oxygen exchange rate as:[45]

$$J(x = 0, t) = k_s \times [\delta(x = 0, t) - \delta(x = 0, \infty)] \tag{3}$$

where J denotes the mass flux, and k_s represents the rate constant. As illustrated, eq 3 indicates that the surface reaction rate is proportional to the difference between the surface oxygen deficiency at the new equilibrium, $\delta(x = 0, \infty)$, and the transient surface oxygen deficiency, $\delta(x = 0, t)$. For the entire exsolution process, we assume k_s to be constant in this model. We are aware that such an assumption is oversimplified because materials' k_s values can significantly increase as a function of metal exsolution.[9,40] Nevertheless, we adopt such an assumption for the simplicity of analytical analysis and expect it will not fundamentally change the modeling results. Meanwhile, we assume the oxygen exchange between the thin film and the substrate is negligible:

$$J(x = d, t) = 0 \tag{4}$$

Since the thickness of the thin-film samples in this study (<60 nm) is well below the critical thickness for STF (~200 μm[44]), the reduction process is limited by the rate of surface oxygen exchange reactions rather than that of bulk oxygen diffusion.[45] As such, the oxygen concentration across the film should remain uniform during lattice reduction, without developing an oxygen concentration gradient in the direction of mass transport (see Figure 2a):

$$\delta(x, t) = \delta(t), \ 0 \le x \le d \tag{5}$$

Note that by using eq 5, we have neglected the chemical inhomogeneity at the topmost surface layer (i.e., $x = 0$) in the STF thin films, where a higher oxygen deficiency may present.[35,46] We expect such simplification will not be critical because we can account for this higher surface reducibility by varying other coefficients in eq 2 (such as c and δ_1).

Under the assumptions described above, the relationship between the time-dependent oxygen deficiency ($\delta(t)$) in the thin-film sample, surface oxygen exchange coefficient (k_s), sample thickness (d), and the reduction time (t) can be written as:[45]

$$\frac{\delta(t) - \delta_0}{\delta_\infty - \delta_0} = 1 - \exp\left(-\frac{k_s}{d}t\right) \tag{6}$$

The exponential time dependence of $\delta(t)$ is shown in Figure 2c, where t_1 denotes the duration of the prereduction step prior to the exsolution onset (see Figure 2b). From eq 6 we can tell that d/k_s is the characteristic time for oxygen exchange in the thin-film samples. Large d/k_s values correspond to slow oxygen release kinetics in the thin-film sample.

Combining eqs 2−6, we modeled the kinetics of prereduction and metal exsolution at different values of d/k_s (i.e., as a function of oxygen release kinetics), and the results are summarized in Figure 2d,e. In the modeling, we set the critical oxygen deficiency in exsolution, δ_1, to be $(\delta_\infty + \delta_0)/2$. Nevertheless, such numerical setting should not affect the generality of the results. As illustrated in Figure 2d, increased values of d/k_s (i.e., slower oxygen release kinetics) increase the pre-reduction period, which delays the onset of metal exsolution. This is because with slow oxygen release kinetics, it takes a longer time for STF to reach the critical oxygen deficiency (δ_1) for the onset of metal exsolution. To compare the kinetics of nanoparticle exsolution, we plot the intensity of exsolved metal as a function of the elapsed time after the exsolution onset in Figure 2e. Since the exsolved metal quantity is dependent on the degree of oxygen deficiency in STF (eq 2), sluggish oxygen release kinetics also make the

https://doi.org/10.1021/jacs.2c10256
J. Am. Chem. Soc. XXXX, XXX, XXX−XXX

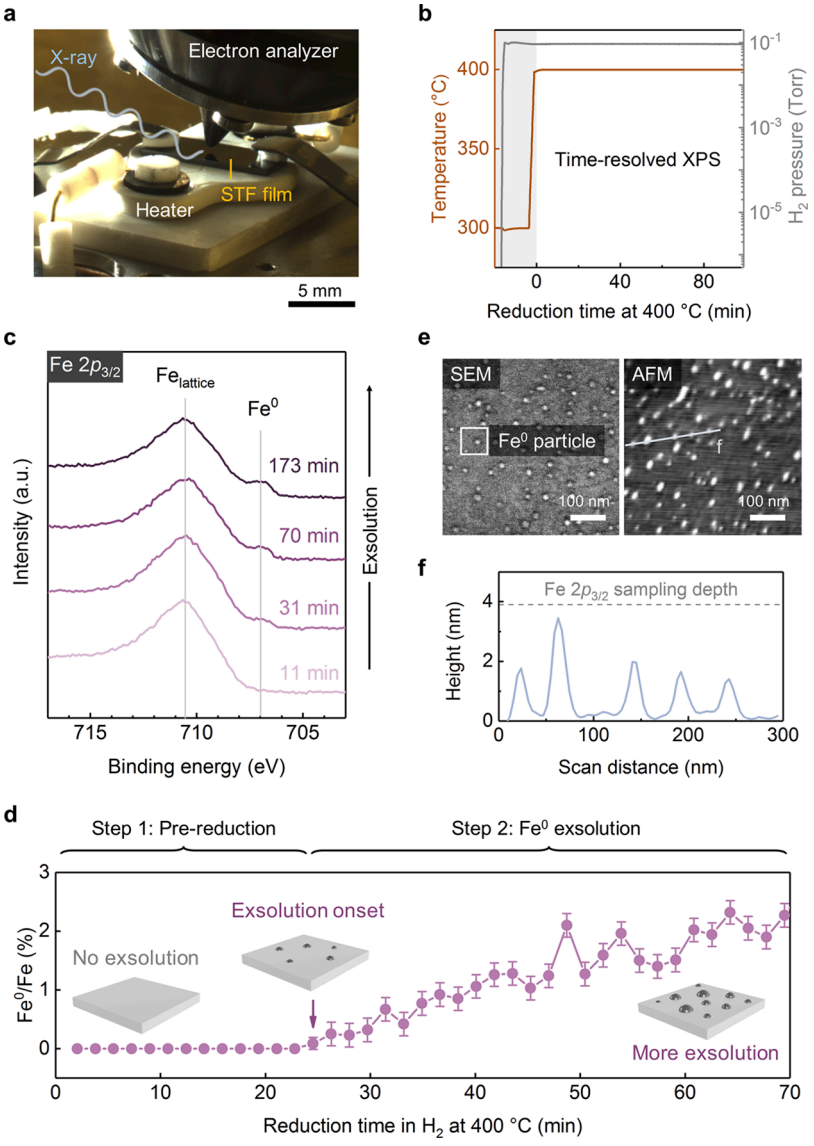

Figure 3. Probing the surface exsolution kinetics with NAP-XPS. (a) Experimental setup of the time-resolved NAP-XPS experiment. (b) Temperature/pressure profiles during the measurement. (c) Representative in situ Fe $2p_{3/2}$ spectra of the STF film as a function of the reduction time at 400 °C in 0.1 Torr H_2. (d) NAP-XPS quantified surface concentration of Fe^0 as a function of the H_2 reduction time. Note the kinetics of both the prereduction step and the Fe^0 exsolution processes can be nicely captured with the time-resolved NAP-XPS measurements. (e) Representative SEM and AFM images showing the surface morphology of the STF film after the NAP-XPS measurement. (f) AFM topology profile of the surface nanoparticles, which is quantified from the solid line in Figure 3e. Note that the particle heights are smaller than the sampling depth of Fe $2p_{3/2}$ NAP-XPS spectra. All the data were collected on the 60 nm STF (001) film.

exsolution process slower. Therefore, our kinetic model indicates that if the kinetics of nanoparticle exsolution is controlled by the oxygen release process (i.e., surface-limited), one should be able to accelerate the exsolution kinetics by reducing the sample thickness (d) and/or increasing the surface reactivity (i.e., increase in k_s).

Cation Diffusion-Limited Exsolution Kinetics. We next take a look at another scenario where the time-dependent quantity, the exsolved metal ($I(t)$), is solely determined by the metal cation diffusion. The analytical solution under this situation has been derived by Gao et al. using a semi-infinite diffusion model.[28] The obtained relationship is shown below:

$$I(t) = a\sqrt{D_c(t - t_1)} \propto \sqrt{t - t_1} \quad (7)$$

where D_c denotes the cation diffusivity, which is assumed to be constant throughout the entire exsolution process. $(t - t_1)$ represents the elapsed time after the exsolution onset. Meanwhile, a represents the constant coefficient.

Note that under our experimental conditions, the exsolution-induced Fe-depletion is highly localized to the STF surface[34] (of around 2 nm). Therefore, given that the Fe concentration in the STF bulk remained largely invariant during exsolution,[34] and that the film thickness is much larger than the exsolution-induced Fe-deficient layer (i.e., $d \gg d^*$), we expect the semi-infinite diffusion model by Gao et al. to be valid in describing the Fe diffusion process in the STF films used in this study. As such, we can conclude from eq 7 that if the exsolution kinetics is completely diffusion-limited, it should be independent of film thickness (d) and surface reactivity (k_s).

https://doi.org/10.1021/jacs.2c10256
J. Am. Chem. Soc. XXXX, XXX, XXX−XXX

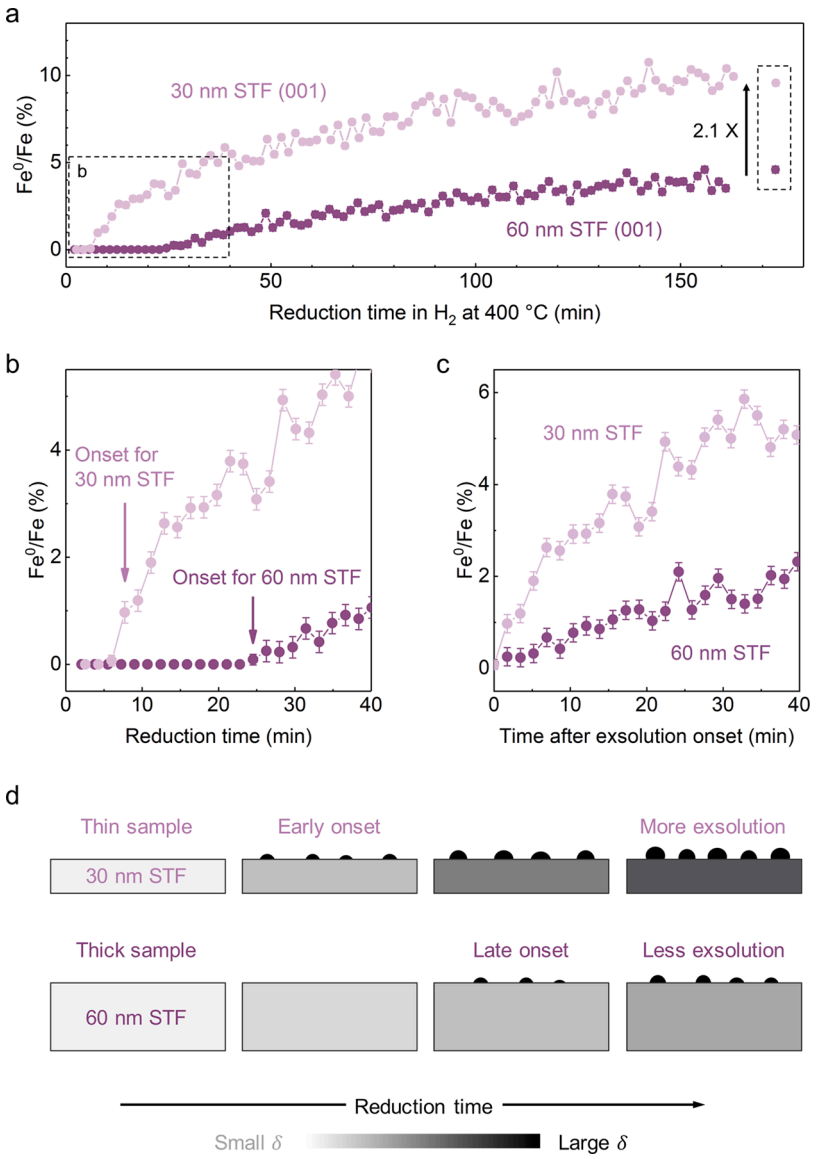

Figure 4. Thickness-dependent exsolution kinetics. (a) Surface Fe^0 concentration on the 30 and 60 nm STF (001) films as a function of H_2 reduction time at 400 °C. (b) Zoom-in plot of Figure 4a showing the 30 nm STF film has an earlier exsolution onset than the 60 nm STF film. (c) Surface Fe^0 concentration as a function of the elapsed time after exsolution onset, which shows that the Fe^0 exsolution kinetics on the 30 nm STF is faster than that of the 60 nm STF film. (d) Proposed mechanism for the thickness-dependent exsolution kinetics. The thinner STF sample can reach higher oxygen deficiency (δ) quicker upon reduction, which results in an earlier exsolution onset, and more exsolved Fe^0 over time.

RESULTS AND DISCUSSION

As elucidated above, we can differentiate between surface- and diffusion-limited exsolution kinetics by examining the dependence of the exsolution kinetics on film thicknesses and the surface oxygen exchange reactivity. In the following sections, we confirm with time-resolved NAP-XPS that by reducing the film thickness or increasing the surface reactivity, one can effectively accelerate the exsolution kinetics on the STF surfaces. These experimental observations agree well with the surface-limited kinetic model shown in Figure 2.

Probing Exsolution Kinetics In Situ with Time-Resolved NAP-XPS. The experimental setup for the NAP-XPS measurements is shown in Figure 3a. As shown in Figure 3b and described in more detail in Methods, we rapidly heated the STF sample to 400 °C and then probed the Fe^0 exsolution kinetics on the STF surface with in situ NAP-XPS under constant environmental conditions (i.e., 400 °C, 0.1 Torr H_2). The representative in situ NAP-XPS Fe $2p_{3/2}$ spectra of the STF film, as a function of the reduction time at 400 °C, are shown in Figure 3c. As illustrated, the Fe $2p_{3/2}$ spectra can be decomposed into the lattice Fe ($Fe_{lattice}$) and metallic Fe (Fe^0) components[35,40] (see Figure S1). The most important feature to note in Figure 3c is the appearance and growth of surface Fe^0 species, which originate from an increasing extent of Fe^0 exsolution upon prolonged reduction by H_2.[21,34,39] On the other hand, the peak shapes of other core-level NAP-XPS spectra (i.e., O 1*s*, Ti 2*p*, and Sr 3*d*) remained stable during Fe^0 exsolution (Figure S2).

The representative time-dependent Fe^0 concentration (i.e., $Fe^0/(Fe^0 + Fe_{lattice})$) on the STF surface is shown in Figure 3d. In this plot, time zero denotes the time that the sample first reached 400 °C in the H_2 gas (see Figure 3b). Meanwhile, we consider the time when Fe^0 signals first appeared in NAP-XPS (indicated by the arrow in Figure 3d) to be the exsolution

https://doi.org/10.1021/jacs.2c10256
J. Am. Chem. Soc. XXXX, XXX, XXX−XXX

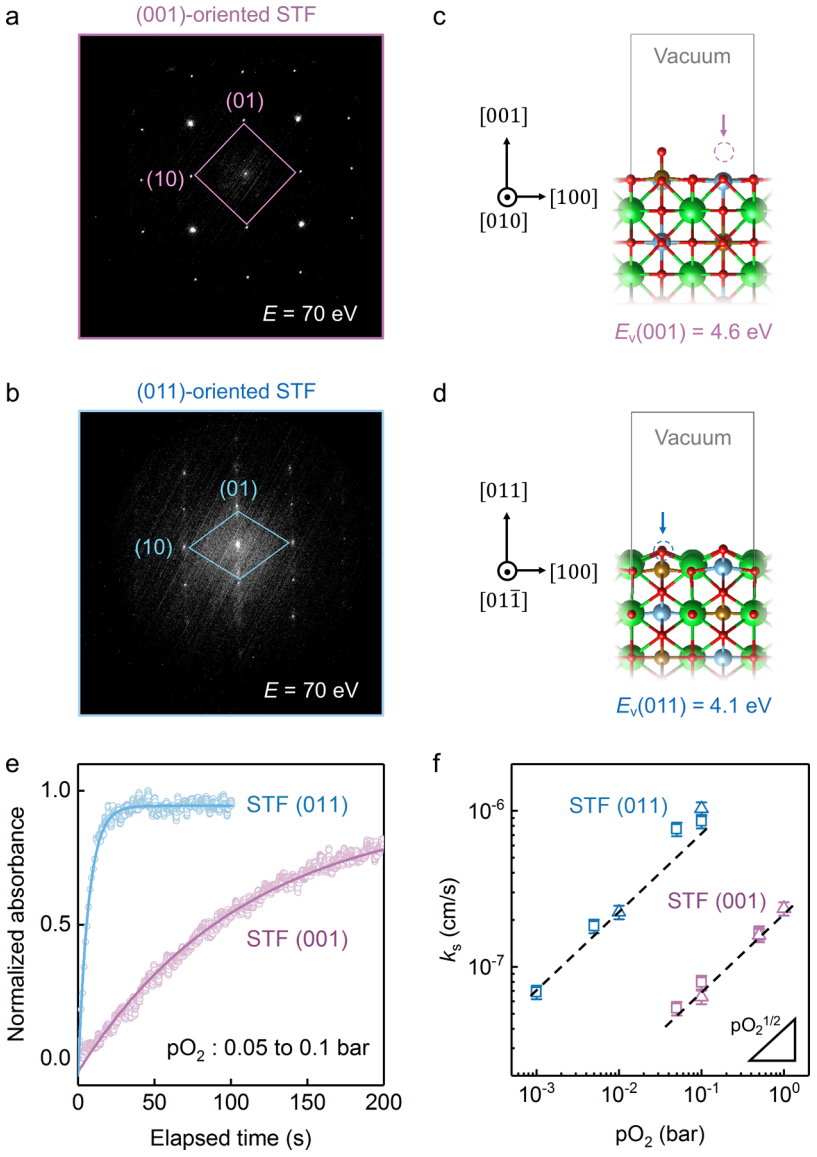

Figure 5. Orientation-dependent surface structure, reducibility, and reactivity of STF. (a,b) Low-energy electron diffraction (LEED) patterns of the as-prepared STF (001) and STF (011) films, respectively. The solid boxes highlight the $p(1 \times 1)$ unit cell. (c,d) Atomic structures and the corresponding oxygen vacancy formation energy (E_v) of the (c) (Ti,Fe)O-terminated STF (001) surface and (d) O_2-terminated STF (011) surface. As illustrated, the STF (011) surface is more reducible than STF (001). The oxygen vacancy positions are highlighted with arrows. Color codes: green, Sr.; brown, Fe; blue, Ti; red, oxygen. (e) Comparison between the optical absorption relaxation (OAR) curves for the (001)- and (011)-oriented STF films, which were conducted at 600 °C. The scattered symbols and solid lines denote the raw experimental data and the exponential fit, respectively. (f) Comparison between the measured k_s for STF (001) and STF (011) thin films as a function of pO_2 at 600 °C. The square and triangle symbols represent the k_s values that were measured upon lowering and increasing pO_2, respectively. OAR reveals that the oxygen exchange kinetics on the STF (011) surface is faster than that of STF (001).

onset time on the STF surface. This is reasonable because previous NAP-XPS studies have successfully correlated the surface metallic species formation to the surface morphology evolution[41] and surface reactivity enhancement[40] during the exsolution process. Therefore, the elapsed time until the first Fe^0 species appeared on the surface indicates how quickly the film reaches the critical oxygen deficiency (i.e., δ_1 in eq 2) for exsolution. The prereduction period prior to the exsolution onset is characterized by a continuous intensity decrease in the O 1*s* spectra[21] (Figure S3) and a binding energy shift[35] in the XPS spectra (Figure S4), both of which suggest that the STF film kept releasing oxygen upon H_2 reduction. After the exsolution onset, the concentration of surface Fe^0 increases with prolonged reduction time, which reflects the nucleation and growth of exsolved Fe^0 nanoparticles.[41] Therefore, the rate of Fe^0 intensity increase in NAP-XPS can effectively measure the exsolution kinetics.

The representative surface morphology after the NAP-XPS experiment is shown in Figure 3e. As illustrated, surface nanoparticles can be observed from both ex-situ scanning electron microscopy (SEM) and atomic force microscopy (AFM) imaging. Notably, the nanoparticles in the AFM images appear to be larger than those in the SEM images. This is due to the tip convolution effects in the AFM imaging.[47] The topological line profile of the surface nanoparticles from the AFM image is shown in Figure 3f. As can be seen, the heights of the surface nanoparticles are smaller than the sampling depth of the Fe $2p_{3/2}$ spectra in our experiments (~4 nm at

https://doi.org/10.1021/jacs.2c10256
J. Am. Chem. Soc. XXXX, XXX, XXX−XXX

1270 eV photon energy, see Figure S5). Furthermore, due to the tip convolution effect[47] and the volume expansion[48] upon Fe^0 nanoparticle reoxidation in air,[21,34,39] the as-exsolved Fe^0 nanoparticles should be even smaller than those that appeared in the ex-situ AFM images. Therefore, NAP-XPS should probe the entire volume of the exsolved Fe^0 nanoparticles. As such, the Fe^0 intensities in the Fe $2p_{3/2}$ spectra should directly reflect the total quantities of exsolved Fe^0 atoms on the STF surface. In particular, given the 80 μm × 20 μm spot size of the X-ray[38] and the $>10^{10}$ cm^{-2} particle density (Figure 3e), we can simultaneously track the averaged exsolution kinetics of $\sim 10^6$ nanoparticles on the STF surface.

Reduced Film Thickness Accelerates Exsolution. Using the experimental protocol described above, we first examine whether reduced film thickness can also accelerate the Fe^0 exsolution kinetics in STF, as predicted by the surface-limited kinetic model in Figure 2d,e. For this purpose, we prepared 30 and 60 nm (001)-oriented STF (001) (Figure S6) and used time-resolved NAP-XPS measurements to compare the exsolution kinetics of these two samples (Figure 4a). As a result, in accordance to the surface-limited kinetic model in Figure 2, we found that the Fe^0 exsolution kinetics on the 30 nm STF film are much faster than that of the 60 nm STF film.

First, as highlighted in Figure 4b, the 30 nm STF film exhibits an earlier exsolution onset than that of the 60 nm STF film. The decrease in the prereduction time on the 30 nm STF can be explained using eq 6, which shows that the time required to reach the critical oxygen deficiency (δ_1) for exsolution is smaller for samples with reduced thickness. Second, after the same amount of reduction time after the exsolution onset, the 30 nm STF film exsolved more Fe^0 than the 60 nm STF (Figure 4c), suggesting the Fe^0 species were produced at a higher rate on the 30 nm STF surface. Consequently, after a 3-h H_2 reduction at 400 °C, the 30 nm STF film exsolved more than twice as much of Fe^0 than that of the 60 nm STF film (Figures 4a and S7). The larger Fe^0 exsolution quantity on the 30 nm STF was also confirmed via ex-situ SEM (Figures S8 and S9).

This observation may look surprising at the first glance: given the same exsolution conditions and identical structure and surface chemistry of materials, how could a thinner sample exsolve more metal over time than a thicker one? The proposed mechanism behind the thickness-dependent exsolution is schematically shown in Figure 4d. As predicted by eq 6, thinner STF samples can reach higher oxygen deficiency (δ) quicker upon reduction, which results in an earlier exsolution onset, and more exsolved Fe^0 over time compared to their thicker counterpart. Note that the earlier exsolution onset and faster Fe^0 formation rate also agree well with the analytical model for the surface-limited exsolution (Figure 2d,e).

On the other hand, had the exsolution kinetics been completely determined by the cation diffusion in STF, the exsolution kinetics for STF samples with different thicknesses should behave exactly the same (as suggested by eq 7). Therefore, the seemingly counterintuitive observations in Figure 4a–c in fact provide a strong piece of evidence that the exsolution kinetics is not solely determined by the cation diffusion in host oxides. Rather, the oxygen release process in host oxides should play a crucial role in determining the exsolution kinetics.

Enhanced Surface Reactivity Accelerates Exsolution. Having shown that reducing the film thickness can accelerate exsolution, we next examine the second hypothesis of this study: Can we boost the exsolution kinetics by increasing the surface reactivity k_s? Since orientation engineering provides a compositional- and strain-independent approach to tailor materials' surface reactivity,[36,37,49] in this section, we investigate the Fe^0 exsolution kinetics on 60 nm (001)- and (011)-oriented STF films that have different k_s values. As a result, we found that the STF (011) surface that has a higher surface reactivity also exhibits accelerated exsolution kinetics, which supports our hypothesis and is in agreement with our analytical modeling (Figure 2).

The surface and bulk lattice orientations of the STF (001) and STF (011) films were confirmed by electron (Figure 5a,b) and X-ray diffraction (XRD) (Figure S10), respectively. Due to the very similar lattice parameter between the STF film and the $SrTiO_3$ (STO) substrate, we can safely rule out the strain effect[21] on exsolution in this study (Figure S10). In addition, these two surfaces have nearly identical roughness (Figure S11) and chemical compositions (Figure S12), making them ideal model systems to investigate the orientation effect on exsolution. Since materials' capability to form oxygen vacancy on the surface (i.e., surface reducibility) can have great implications on their oxygen exchange reactivity,[46,50,51] we further employed density functional theory (DFT) calculations to compare the oxygen vacancy formation energy (E_v) on the STF (001) and STF (011) surface. Specifically, we focused on the (Ti,Fe)O_2-terminated STF (001) surface (Figure 5c) and the O_2-terminated STF (011) surface (Figure 5d) as they represent the preferred surface termination in each lattice orientation, with both lower surface energies[52,53] and higher surface reducibility than other terminations (Figure S13). We found that the oxygen vacancy formation energy on the STF (011) surface is lower than that of the STF (001), indicating that the STF (011) surface is more reducible. The higher reducibility of the (011)-oriented surface has also been observed on a similar perovskite oxide, $La_{0.8}Sr_{0.2}Co_{0.2}Fe_{0.8}O_3$, where the increased surface reducibility was found to lead to a highly enhanced gas-exchange kinetics on the (011) surface.[36]

To assess the orientation-dependent surface reactivity of STF, we conducted OAR measurements[54,55] on these two samples in the as-prepared form, without Fe^0 exsolution. The representative OAR results for the STF (001) and STF (011) films in O_2 at 600 °C are shown in Figure 5e, which highlights the much faster response of the STF (011) film than that of the STF (001). To quantify the rate constants (k_s) on these two samples, we fit the relative absorbance curves with exponential functions (see eq 10 in Methods). The fitting results are shown with solid lines in Figure 5e. As illustrated, the relaxation curves can be precisely captured by the exponential fittings, which confirms that the oxygen exchange kinetics in STF films are limited by the surface reaction rates, rather than bulk oxygen diffusion.[45]

The obtained rate constants (k_s) on the (001)-oriented and (011)-oriented STF films are shown in Figure 5f as a function of the pO_2 value at the end of each pO_2 step in OAR measurements. In particular, the k_s values that were measured upon up and down pO_2 steps are shown with square and triangle symbols, respectively (see Methods). These two types of k_s measurements nearly overlap, which confirms that the pO_2 steps employed in this study are small enough to enable accurate OAR quantification.[45] As indicated by the dashed lines in Figure 5d, the slope for the $\log(k_s)$– $\log(pO_2)$ relationship is around 1/2 for both types of surface termination. The observed slope in this study is slightly larger

https://doi.org/10.1021/jacs.2c10256
J. Am. Chem. Soc. XXXX, XXX, XXX–XXX

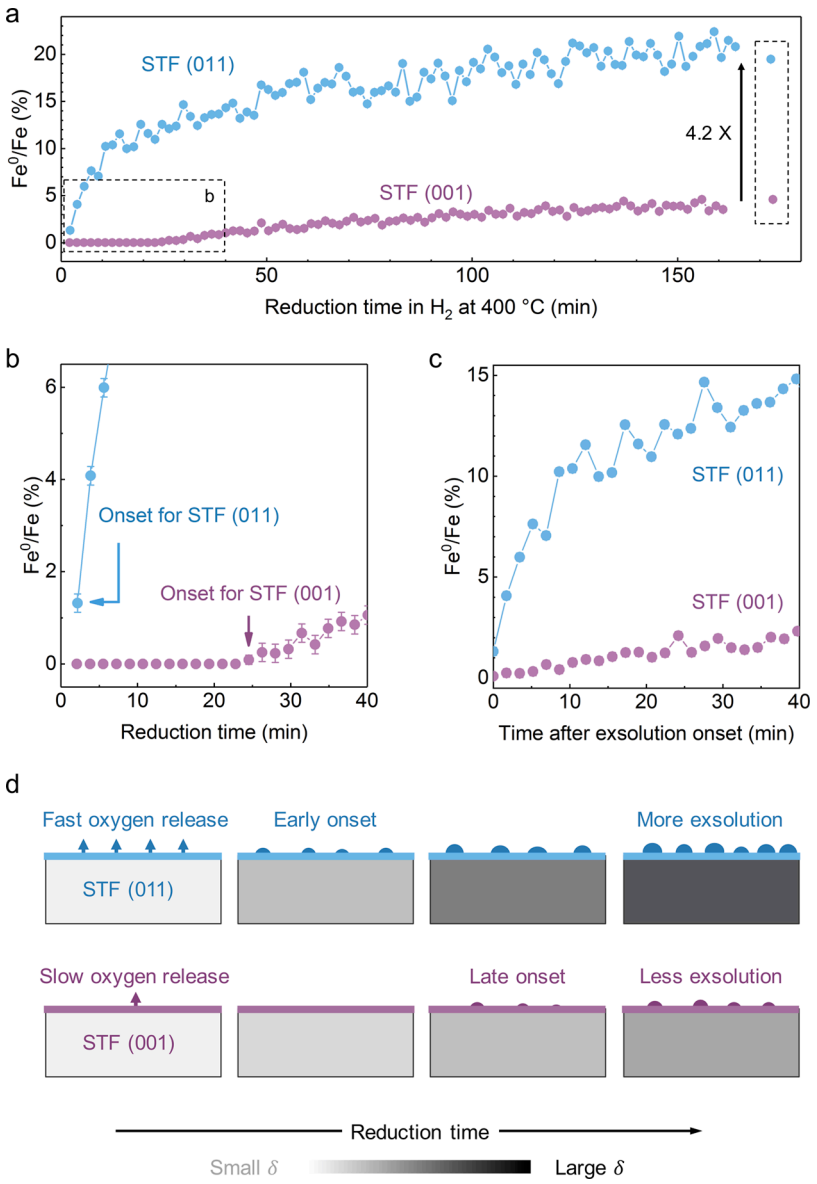

Figure 6. Orientation-dependent exsolution kinetics. (a) Surface Fe^0 concentration on the 60 nm (001)- and (011)-oriented STF films as a function of H_2 reduction time at 400 °C. (b) Zoom-in plot showing STF (011) has an earlier exsolution onset than STF (001). (c) Surface Fe^0 concentration as a function of the elapsed time after exsolution onset, which shows that the Fe^0 exsolution kinetics on STF (011) is faster than that of STF (001). (d) Proposed mechanism for the orientation-dependent exsolution. The (011)-oriented STF sample has a higher surface oxygen release rate, which can reach higher oxygen deficiency (δ) quicker upon reduction. As such, STF (011) has an earlier exsolution onset and can induce more exsolved Fe^0 over time than STF (001).

than those reported in the literature on polycrystalline STF films (~0.3, see refs 44, 56). We expect the differences in the pO_2 dependence to be related to the sample crystallinity, as the STF films used in this work are single-crystalline (Figures 5 and S5). As a result, we concluded that the surface oxygen exchange rates (k_s) on the STF (011) surface are much faster than that of STF (001) in the high pO_2 region (>10^{-3} Torr) at 600 °C. The superior surface reactivity on the (011)-oriented surface likely originates from its high surface reducibility (Figure 5c,d). These findings are also consistent with the literature, where the (011) surfaces are commonly observed to have a higher surface reactivity than the (001) surfaces.[36,49]

In OAR measurements, we relied on the optical signals from electron holes (i.e., the nominal Fe^{4+} species,[57,58] see Methods), which are only present in STF under oxidizing conditions.[57] Therefore, it is challenging to use OAR to quantify k_s under reducing conditions that are more relevant to exsolution. To address this issue, we turned to time-resolved NAP-XPS to directly compare the surface oxygen release rate on these two STF terminations under exsolution-relevant conditions. This approach is viable because higher k_s values help to reach the critical oxygen deficiency (δ_1) more quickly, which will shorten the prereduction time (t_1) prior to the exsolution onset (Figure 2). Therefore, by comparing the reduction time required to onset Fe^0 exsolution on both samples, we can qualitatively compare the surface reactivity between STF (001) and STF (011). The feasibility of using NAP-XPS to track the exsolution onset has been validated in Figure 4, where we successfully resolved the thickness-dependent exsolution onset time on the STF (001) surface.

Figure 6a shows the time-dependent surface concentrations of Fe^0 on the (001)- and (011)-oriented STF films upon

https://doi.org/10.1021/jacs.2c10256
J. Am. Chem. Soc. XXXX, XXX, XXX−XXX

reduction at 400 °C in 0.1 Torr H_2. Notably, the STF (011) sample demonstrates an earlier exsolution onset than STF (001). As shown in Figure 6b, while it took ∼25 min for the first noticeable Fe^0 signal to appear on the STF (001) surface, the Fe^0 species almost immediately appeared on the STF (011) surface once the sample started H_2 reduction at 400 °C (experimental procedure shown in Figure 3b). The huge difference in the exsolution onset time thus provides strong evidence that the STF (011) surface has a higher reactivity than the STF (001) surface in a highly reducing environment. Note that the NAP-XPS observed surface reactivity relationship (i.e., $k_s(011) > k_s(001)$) agrees well with the OAR measurements in Figure 5e,f, although the latter was conducted in the high pO_2 region and at a higher temperature.

After having elucidated the different surface oxygen exchange reactivities of these two samples, we then compared their exsolution kinetics using time-resolved NAP-XPS. In accordance to the faster oxygen release rate of STF (011), the exsolution kinetics on the STF (011) surface is also much faster than that of STF (001). As shown in Figure 6c, after the exsolution onset, the STF (011) surface can exsolve Fe^0 species at a higher rate than the STF (001) surface. As a result, at the end of the NAP-XPS measurement (i.e., after 3-h H_2 reduction at 400 °C), the Fe^0 concentration on the STF (011) surface was more than four times higher than that of the STF (001) surface (Figures 6a and S14). The surface morphologies of the (001)- and (011)-oriented STF films after the NAP-XPS measurements are shown in Figure S15. Consistent with the higher Fe^0 signal on the (011)-oriented STF, the total volume of the exsolved nanoparticles on the STF (011) surface is also larger than that of STF (001) (see Figure S16). The observed orientation-dependent exsolution kinetics can be nicely explained by the different surface reactivities on these two terminations. As illustrated in Figure 6d, as the (011)-oriented STF sample has a higher surface oxygen release rate, it can reach higher oxygen deficiency (δ) quicker upon reduction. As such, STF (011) has both an earlier exsolution onset and generates more Fe^0 over time.

Note that a preferred metal exsolution on the (011) surface has also been found in Ni-doped (La,Sr)TiO_3, but was attributed to the faster cation diffusion in the [011] direction[14] or the reduced interfacial energy between the exsolved metal and the (011) surface.[23] Nevertheless, as will be elaborated below, we show these two factors cannot explain the observed orientation-dependent exsolution in this study. First, as discussed in Figure 4, the Fe^0 exsolution kinetics in the STF films is not rate-limited by the cation diffusion process. Therefore, the potentially enhanced cation diffusivity along the [011] direction[59] cannot explain the accelerated exsolution kinetics on the (011) surface. Second, to compare the interfacial energy between Fe^0 and the STF (001) and (011) surfaces, we quantified the height-to-radius ratio of surface exsolved nanoparticles on these two surfaces (Figure S17). Previous studies have shown that higher interfacial energy can impede exsolution by increasing the nucleation barrier, which will result in exsolved nanoparticles with a larger height-to-radius ratio.[23] Therefore, had the accelerated exsolution kinetics on the STF (011) surface been mainly governed by the reduced interfacial energy (and hence reduced nucleation barrier), the exsolved nanoparticles on the (011) surface should have a smaller height-to-radius ratio than those on the (001) surface. However, we observed exactly the opposite. By quantifying the nanoparticle morphology with AFM (Figure S17), we show that the exsolved Fe^0 particles on the STF (011) surface in fact have a larger height-to-radius ratio than those on STF (001). Therefore, the orientation-dependent exsolution kinetics observed in Figure 6 cannot be explained by the differences in the interfacial energy, either.

Having excluded the potential contributions from cation diffusivity and interfacial energy, and given the nice agreement between the surface-limited analytical modeling with the experimental results, we expect the orientation-dependent surface reactivity to be the primary factor behind the different exsolution kinetics in Figure 6. As such, we confirm that by increasing the surface oxygen exchange reactivity k_s, one can effectively accelerate surface Fe^0 exsolution kinetics on STF.

Enhancing Oxygen Release Kinetics in Materials is Critical to Boost Exsolution. So far, we have experimentally demonstrated that reducing the film thickness (Figure 4) and increasing the surface reactivity (Figure 6) have similar effects in accelerating the surface Fe^0 exsolution kinetics in thin-film STF. Both effects can be well-explained using a unified theoretical framework based on the surface-limited exsolution kinetics (Figure 2). These findings thus indicate that the Fe^0 exsolution kinetics on STF thin films are primarily limited by the surface oxygen release process rather than bulk cation diffusion (eq 7). As such, the key to accelerating Fe^0 exsolution kinetics on the STF surface is to enhance its oxygen release rates.

While our experiments were conducted at 400 °C on thin-film STF, we expect the conclusion is also applicable for surface Fe^0 exsolution that occurs at higher temperatures and from thick/bulk STF materials. First, since the activation energy for the surface oxygen release reactions in STF (∼ 1 eV[60]) is smaller than that of cation diffusion (∼4 eV[43]), the increase in cation diffusivity should be greater than that of the oxygen release kinetics upon raising the temperature. As such, we expect the oxygen release kinetics remain the dominant rate-limiting factor for Fe^0 metal exsolution in STF even at higher temperatures. Therefore, increasing surface oxygen release kinetics should promote Fe^0 exsolution on STF at temperatures above 400 °C. Second, as shown in Figures 2 and 6, increasing the sample thickness will make STF take a longer time to release oxygen till a specific oxygen deficiency (δ) for metal exsolution (eq 2). Meanwhile, the cation diffusion rate is independent of the sample thickness. As a result, the oxygen release process should still be rate-limiting for Fe^0 exsolution on STF samples with a larger thickness. It should be noted that, however, for bulk/thick STF samples that have a thickness larger than the critical thickness[44] (i.e., $d > 200$ μm), the oxygen diffusion kinetics in the bulk[45] can no longer be neglected. To shed light on this situation, we revised the analytical model in Figure 2 by considering an STF sample with infinite thickness. In this case, the time-dependent oxygen deficiency at the host oxide surface ($\delta(x = 0, t)$), which directly dictates the extent of surface metal exsolution (eq 2), is given by:[61]

$$\frac{\delta(x=0,t)-\delta_0}{\delta_\infty-\delta_0} = 1 - \exp\left(\frac{k_s^2}{D_o}t\right)\mathrm{erfc}\left(k_s\sqrt{\frac{t}{D_o}}\right) \quad (8)$$

where D_o denotes the oxygen diffusivity and erfc is the complementary error function. All the other symbols in eq 8 follow the same definitions as in eq 6. As illustrated, the time-dependent surface oxygen deficiency ($\delta(x = 0, t)$), and hence the exsolved metal quantity (see eq 2), are dependent on both

https://doi.org/10.1021/jacs.2c10256
J. Am. Chem. Soc. XXXX, XXX, XXX−XXX

the surface reactivity (k_s) and the oxygen diffusivity (D_o) for bulk STF samples. Nevertheless, even in this scenario, due to its strong dependence on k_s (eq 8), one should be able to accelerate the Fe^0 exsolution kinetics on the surface of thick/bulk STF by increasing their surface oxygen release kinetics.

CONCLUSIONS

It is important to quantify the kinetic rate-limiting processes that govern metal nanoparticle exsolution out of host oxides, so that we can ultimately tune the dispersion of exsolved metal nanoparticles to increase their catalytic activity. This paper has systematically investigated the surface metal exsolution kinetics on model epitaxial thin-film STF as an important model material system for electrochemical energy and fuels conversion. Time-resolved NAP-XPS measurements allowed us to quantify the exsolution kinetics in situ on the STF surfaces, both dynamically and statistically. Analytical kinetic modeling further enabled us to interpret the experiments and to decouple the contributions of surface oxygen release reactions and bulk cation diffusion to the exsolution kinetics. As a result, we found that by enhancing the oxygen release rates on STF, which was achieved by either reducing the sample thickness or by increasing the surface reactivity, one can effectively shorten the prereduction time prior to the exsolution onset. Furthermore, a fast oxygen release rate also increases the kinetics of nanoparticle nucleation and growth, and hence increases the total amount of exsolved Fe^0 over time. These findings unequivocally demonstrated that the Fe^0 exsolution kinetics in STF are primarily limited by the surface oxygen release process (i.e., surface-limited), instead of bulk cation diffusion. While in this study we examined Fe^0 exsolution kinetics at 400 °C using thin-film STF, we expect the conclusions can be generalized to exsolution reactions in STF that occur at higher temperatures and from different materials geometries (such as bulk electrodes). For all the cases described above, increasing the surface oxygen release kinetics in STF should promote surface Fe^0 exsolution.

Since different host oxides can have dramatically different surface oxygen exchange rates,[51,62] we are aware that the observed surface-limited exsolution kinetics in STF may not apply to all types of host oxides. Nevertheless, the experimental and analytical methods presented in this study are broadly applicable to help identify the rate-limiting step(s) in exsolution for many other materials systems. Moreover, the results we obtained from STF clearly highlight the need to consider the previously overlooked oxygen release kinetics in designing exsolved nanocatalysts. For exsolution reactions that are limited by the surface oxygen release kinetics in host oxides, this work also provides practical guidance to promote metal exsolution. For example, instead of using bulk materials as host oxides, employing thin films or surface coatings to exsolve from them should be more desirable. Moreover, applying surface treatments to enhance the surface oxygen exchange reactivity, such as surface doping[63] and modifying the surface acidity[62,64] and termination,[51] can also be promising approaches to tailor nanoparticle exsolution.

METHODS

Sample Preparation. Thin-film STF was deposited using pulsed laser deposition (PLD) with a KrF (λ = 248 nm) excimer laser on (001)- and (011)-oriented 10 × 5 × 0.5 mm 0.7% Nb-doped STO single crystal substrates (MTI Corporation, 1-side polished). For the optical studies, (001)- and (011)-oriented, two-side polished, 10 × 10 × 0.5 mm, STO single crystal substrates (MTI Corporation) were used. During the PLD process, the substrate temperature was kept at 815 °C in an oxygen pressure of 0.5 mTorr. By applying 4000 or 8000 laser pulses (2 Hz, 400 mJ), a STF thin film of around 30 nm to 60 nm thickness was grown on the substrate. More detailed descriptions on the sample preparation and film characterization can be found in our earlier study.[34]

NAP-XPS Measurement. The in situ NAP-XPS measurements were carried out at the IOS (23-ID-2) beamline[38] of the National Synchrotron Light Source II (NSLS-II) at Brookhaven National Lab. The sample was placed on a pyrolytic boron nitride heater, with a K-type thermocouple mounted directly onto the sample surface for temperature measurements. To be able to directly compare the experimental results to the kinetic models described in the Theory section, we designed the experimental procedure as follows to probe the exsolution kinetics of the STF films upon nearly step-change reduction (see Figure 3b).

For each time-dependent NAP-XPS measurement, the STF films were first preconditioned at 300 °C in 20 mTorr O_2 to remove the adventitious carbon (Figure S18). Then, while maintaining the sample temperature at 300 °C, the chamber was pumped down to vacuum ($<10^{-7}$ Torr). After that, we introduced 0.1 Torr H_2 to the NAP-XPS chamber. Note that the 300 °C temperature was chosen so that no exsolution would occur at this condition (Figure S19). As such, we can have the time to stabilize the gas pressure in the chamber. Finally, we heated the STF films in 0.1 Torr H_2 to 400 °C at a heating rate of 40 °C/min. A rapid heating rate was employed to ensure that negligible exsolution would take place before reaching 400 °C. Once the sample temperature reached 400 °C, we started to collect in situ NAP-XPS data continuously on the sample for 3 h. The photon energies for all the measurements were set to be 1270 eV. All the NAP-XPS spectra were quantified with CasaXPS.[65] The XPS peaks are fitted with a 30% Lorentz/Gaussian line shape over a Shirley background. If not specified, the binding energy of all the spectra displayed in this paper were calibrated by aligning the Ti $2p_{3/2}$ peak at 458.4 eV.

Thin-Film Characterization. AFM images were collected using a Cypher S AFM Microscope with tapping mode. The AFM tips used were AC160TS-R3 from Oxford Instruments. The AFM characterization was done on the center of the sample to avoid edge effects. All the AFM images were analyzed with the Gwyddion software.[66] Lab-based XRD data were measured with a Rigaku SmartLab X-ray diffractometer using Cu *K*-alpha 1 radiation. SEM images were collected with the FEI Helios Nanolab 600 Dual Beam System, using the Immersion mode. The LEED measurement was conducted at the X-ray photoemission electron microscopy/LEEM endstation of the electron spectro-microscopy (ESM) beamline (21-ID) of the NSLS-II. To remove surface contamination, the LEED measurements were conducted at room temperature after the STF film was annealed in 10^{-5} Torr O_2 at 400 °C for 15 min, without exposing the sample to air.

OAR Measurements. The OAR technique measures the oxygen exchange kinetics by probing the time relaxation in the light intensity transmitted through the STF film as it becomes more oxidized (more strongly absorbing in the visible due to an increase in Fe^{4+} concentration) or reduced (decrease in Fe^{4+} concentration) in response to step changes in oxygen partial pressure (pO_2), according to the defect model.[58] The OAR measurements were conducted using a custom-made near infrared−VIS−UV transmission spectrophotometer, capable of in situ measurements at elevated temperature and in a controlled gas environment, as described in detail elsewhere.[67] The gas composition (and pO_2) of the atmosphere inside the optical flow cell was controlled by a constant flow (at rate of 140 sccm) of premixed pure O_2 and Ar gases. The pO_2 steps were created by automated changes in the O_2/Ar ratio, keeping the flow rate constant.

During the OAR measurement, we continuously monitored the optical transmittance at a wavelength of 470 ± 2 nm, which falls within the absorption spectrum region of Fe^{4+} cations in STF,[57,58] but sufficiently far away from the absorption due to excitations across the band gap. As exemplified by the optical transmittance spectra in

https://doi.org/10.1021/jacs.2c10256
J. Am. Chem. Soc. XXXX, XXX, XXX−XXX

Figure S20, the STF film exhibits decreased light transmittance when it becomes oxidized. Therefore, each pO_2 step-change leads to the transition to a new optical absorption state, as determined by the defect kinetics in STF.[58] The change in absorbance (relative absorbance) during pO_2 step-changes was calculated via an approximate relation

$$\Delta A = \ln\left(\frac{T}{T_0}\right) \tag{9}$$

where T_0 and T represent the sample's transmittances in the reference and the transient states, respectively. For sufficiently small pO_2 steps, and for surface exchange reaction-limited kinetics, the evolution of the relative absorbance as a function of time is described by:[55,58]

$$\Delta A(t) = \Delta A_{f-i}\left(1 - \exp\left(-\frac{k_s}{d}t\right)\right) \tag{10}$$

where ΔA_{f-i} denotes a difference in absorbance at equilibrium, before and after the pO_2 step.

DFT. DFT calculations were performed with the Vienna Ab-initio Simulation Package.[68] An energy cut-off of 500 eV was used with the Perdew−Burke−Ernzerhof functional and the generalized gradient approximation. A Hubbard U correction of 4.0 eV was applied to Fe. All calculations were spin-polarized. Bulk calculations are done using a 2 × 2 × 2 STO supercell (8 formula units with a 4 × 4 × 4 K-point grid). For the surface calculations, we constructed surface slabs with ten atomic layers and 20 Å of vacuum. Atoms of the five bottom layers were fixed while the top surface was allowed to relax. A 1 × 1 × 1 K-point grid was used. The oxygen formation energies are calculated as the energy difference between the surface containing one oxygen vacancy and the perfect surface.

■ ASSOCIATED CONTENT

Supporting Information

The Supporting Information is available free of charge at https://pubs.acs.org/doi/10.1021/jacs.2c10256.

XPS analysis, additional sample characterization, evolution of the Ti-normalized surface, binding energy shift in XPS during the prereduction stage, probing depth of NAP-XPS, thickness calibration of the 30 nm STF film, comparison of the Fe 2p spectra, surface morphologies after the NAP-XPS experiments, comparison of the exsolved particle volume, bulk structures of the STF films, surface morphology of the as-prepared STF films, surface chemical composition of the as-prepared STF films, optical relaxation measurements, DFT calculation, and morphology of the exsolved nanoparticles (PDF)

■ AUTHOR INFORMATION

Corresponding Author

Bilge Yildiz − *Department of Nuclear Science and Engineering and Department of Materials Science and Engineering, Massachusetts Institute of Technology, Cambridge, Massachusetts 02139, United States;* orcid.org/0000-0002-2688-5666; Email: byildiz@mit.edu

Authors

Jiayue Wang − *Department of Nuclear Science and Engineering, Massachusetts Institute of Technology, Cambridge, Massachusetts 02139, United States;* orcid.org/0000-0002-2027-3634

Dmitri Kalaev − *Department of Materials Science and Engineering, Massachusetts Institute of Technology, Cambridge, Massachusetts 02139, United States*

Jing Yang − *Department of Materials Science and Engineering, Massachusetts Institute of Technology, Cambridge, Massachusetts 02139, United States;* orcid.org/0000-0003-1855-0708

Iradwikanari Waluyo − *National Synchrotron Light Source II, Brookhaven National Laboratory, Upton, New York 11973, United States;* orcid.org/0000-0002-4046-9722

Adrian Hunt − *National Synchrotron Light Source II, Brookhaven National Laboratory, Upton, New York 11973, United States;* orcid.org/0000-0002-5283-9647

Jerzy T. Sadowski − *Center for Functional Nanomaterials, Brookhaven National Laboratory, Upton, New York 11973, United States;* orcid.org/0000-0002-4365-7796

Harry L. Tuller − *Department of Materials Science and Engineering, Massachusetts Institute of Technology, Cambridge, Massachusetts 02139, United States*

Complete contact information is available at: https://pubs.acs.org/10.1021/jacs.2c10256

Notes

The authors declare no competing financial interest.

■ ACKNOWLEDGMENTS

The authors thank the OxEon Corporation for supporting this work. This research used the resources of the IOS (23-ID-2) beamline of the NSLS-II and the ESM (21-ID) beamline of the NSLS-II and the Center for Functional Nanomaterials, U.S. Department of Energy (DOE) Office of Science User Facilities operated for the DOE Office of Science by Brookhaven National Laboratory under Contract No. DE-SC0012704. The authors acknowledge the facility support from the Center for Materials Science and Engineering at MIT (NSF under award number DMR-1419807). J.W. thanks Dr. Huanhuan Tian (MIT) for the helpful discussions on the kinetic modeling.

■ REFERENCES

(1) Lee, W.; Han, J. W.; Chen, Y.; Cai, Z.; Yildiz, B. Cation Size Mismatch and Charge Interactions Drive Dopant Segregation at the Surfaces of Manganite Perovskites. *J. Am. Chem. Soc.* **2013**, *135*, 7909−7925.

(2) Kim, D.; Bliem, R.; Hess, F.; Gallet, J.-J.; Yildiz, B. Electrochemical Polarization Dependence of the Elastic and Electrostatic Driving Forces to Aliovalent Dopant Segregation on LaMnO3. *J. Am. Chem. Soc.* **2020**, *142*, 3548−3563.

(3) Lin, R.; et al. Anomalous metal segregation in lithium-rich material provides design rules for stable cathode in lithium-ion battery. *Nat. Commun.* **2019**, *10*, 1650.

(4) Luo, D.; Fang, S.; Tamiya, Y.; Yang, L.; Hirano, S.-i. Countering the Segregation of Transition-Metal Ions in $LiMn_{1/3}Co_{1/3}Ni_{1/3}O_2$ Cathode for Ultralong Life and High-Energy Li-Ion Batteries. *Small* **2016**, *12*, 4421−4430.

(5) Kousi, K.; Tang, C.; Metcalfe, I. S.; Neagu, D. Emergence and Future of Exsolved Materials. *Small* **2021**, *17*, No. 2006479.

(6) Neagu, D.; Tsekouras, G.; Miller, D. N.; Ménard, H.; Irvine, J. T. S. In situ growth of nanoparticles through control of non-stoichiometry. *Nat. Chem.* **2013**, *5*, 916−923.

(7) Nishihata, Y.; et al. Self-regeneration of a Pd-perovskite catalyst for automotive emissions control. *Nature* **2002**, *418*, 164−167.

(8) Myung, J.-h.; Neagu, D.; Miller, D. N.; Irvine, J. T. S. Switching on electrocatalytic activity in solid oxide cells. *Nature* **2016**, *537*, 528−531.

(9) Opitz, A. K.; et al. Understanding electrochemical switchability of perovskite-type exsolution catalysts. *Nat. Commun.* **2020**, *11*, 4801.

(10) Fan, W.; et al. Anodic Shock-Triggered Exsolution of Metal Nanoparticles from Perovskite Oxide. *J. Am. Chem. Soc.* **2022**, *144*, 7657−7666.
(11) Liang, M.; et al. A New Durable Surface Nanoparticles-Modified Perovskite Cathode for Protonic Ceramic Fuel Cells from Selective Cation Exsolution under Oxidizing Atmosphere. *Adv. Mater.* **2022**, *34*, No. 2106379.
(12) Neagu, D.; et al. Demonstration of chemistry at a point through restructuring and catalytic activation at anchored nanoparticles. *Nat. Commun.* **2017**, *8*, 1855.
(13) Jennings, D.; Ricote, S.; Santiso, J.; Caicedo, J.; Reimanis, I. Effects of exsolution on the stability and morphology of Ni nanoparticles on BZY thin films. *Acta Mater.* **2022**, *228*, No. 117752.
(14) Neagu, D.; et al. Nano-socketed nickel particles with enhanced coking resistance grown in situ by redox exsolution. *Nat. Commun.* **2015**, *6*, 8120.
(15) Neagu, D.; et al. In Situ Observation of Nanoparticle Exsolution from Perovskite Oxides: From Atomic Scale Mechanistic Insight to Nanostructure Tailoring. *ACS Nano* **2019**, *13*, 12996−13005.
(16) Yu, S.; et al. Metal Nanoparticle Exsolution on a Perovskite Stannate Support with High Electrical Conductivity. *Nano Lett.* **2020**, *20*, 3538−3544.
(17) Lv, H.; et al. In Situ Investigation of Reversible Exsolution/Dissolution of CoFe Alloy Nanoparticles in a Co-Doped $Sr_2Fe_{1.5}Mo_{0.5}O_{6-\delta}$ Cathode for CO_2 Electrolysis. *Adv. Mater.* **2020**, *32*, No. 1906193.
(18) Lv, H.; et al. Promoting exsolution of RuFe alloy nanoparticles on $Sr_2Fe_{1.4}Ru_{0.1}Mo_{0.5}O_{6-\delta}$ via repeated redox manipulations for CO_2 electrolysis. *Nat. Commun.* **2021**, *12*, 5665.
(19) Hamada, I.; Uozumi, A.; Morikawa, Y.; Yanase, A.; Katayama-Yoshida, H. A Density Functional Theory Study of Self-Regenerating Catalysts $LaFe_{1-x}M_xO_{3-y}$ (M = Pd, Rh, Pt). *J. Am. Chem. Soc.* **2011**, *133*, 18506−18509.
(20) Kwon, O.; et al. Exsolution trends and co-segregation aspects of self-grown catalyst nanoparticles in perovskites. *Nat. Commun.* **2017**, *8*, 15967.
(21) Wang, J.; et al. Tuning Point Defects by Elastic Strain Modulates Nanoparticle Exsolution on Perovskite Oxides. *Chem. Mater.* **2021**, *33*, 5021−5034.
(22) Kim, H.; et al. Unveiling the key factor for the phase reconstruction and exsolved metallic particle distribution in perovskites. *Nat. Commun.* **2021**, *12*, 6814.
(23) Kim, K. J.; et al. Facet-Dependent in Situ Growth of Nanoparticles in Epitaxial Thin Films: The Role of Interfacial Energy. *J. Am. Chem. Soc.* **2019**, *141*, 7509−7517.
(24) Han, H.; et al. Lattice strain-enhanced exsolution of nanoparticles in thin films. *Nat. Commun.* **2019**, *10*, 1471.
(25) Kim, J. K.; et al. Exceptional Tunability over Size and Density of Spontaneously Formed Nanoparticles via Nucleation Dynamics. *ACS Appl. Mater. Interfaces* **2020**, *12*, 24039−24047.
(26) Cuenya, B. R. Synthesis and catalytic properties of metal nanoparticles: Size, shape, support, composition, and oxidation state effects. *Thin Solid Films* **2010**, *518*, 3127−3150.
(27) Jo, Y.-R.; et al. Growth Kinetics of Individual Co Particles Exsolved on $SrTi_{0.75}Co_{0.25}O_{3-\delta}$ Polycrystalline Perovskite Thin Films. *J. Am. Chem. Soc.* **2019**, *141*, 6690−6697.
(28) Gao, Y.; Chen, D.; Saccoccio, M.; Lu, Z.; Ciucci, F. From material design to mechanism study: Nanoscale Ni exsolution on a highly active A-site deficient anode material for solid oxide fuel cells. *Nano Energy* **2016**, *27*, 499−508.
(29) Jiang, G.; Yan, F.; Wan, S.; Zhang, Y.; Yan, M. Microstructure evolution and kinetics of B-site nanoparticle exsolution from an A-site-deficient perovskite surface: a phase-field modeling and simulation study. *Phys. Chem. Chem. Phys.* **2019**, *21*, 10902−10907.
(30) Ferrari, A.; Körmann, F. Surface segregation in Cr-Mn-Fe-Co-Ni high entropy alloys. *Appl. Surf. Sci.* **2020**, *533*, No. 147471.
(31) Jung, W.; Tuller, H. L. A New Model Describing Solid Oxide Fuel Cell Cathode Kinetics: Model Thin Film $SrTi_{1-x}Fe_xO_{3-\delta}$ Mixed Conducting Oxides−a Case Study. *Adv. Energy Mater.* **2011**, *1*, 1184−1191.
(32) Sediva, E.; Defferriere, T.; Perry, N. H.; Tuller, H. L.; Rupp, J. L. M. In Situ Method Correlating Raman Vibrational Characteristics to Chemical Expansion via Oxygen Nonstoichiometry of Perovskite Thin Films. *Adv. Mater.* **2019**, *31*, No. 1902493.
(33) Nenning, A.; Navickas, E.; Hutter, H.; Fleig, J. Water-Induced Decoupling of Tracer and Electrochemical Oxygen Exchange Kinetics on Mixed Conducting Electrodes. *J. Phys. Chem. Lett.* **2016**, *7*, 2826−2831.
(34) Wang, J.; et al. Exsolution-Driven Surface Transformation in the Host Oxide. *Nano Lett.* **2022**, *22*, 5401−5408.
(35) Nenning, A.; et al. Ambient Pressure XPS Study of Mixed Conducting Perovskite-Type SOFC Cathode and Anode Materials under Well-Defined Electrochemical Polarization. *J. Phys. Chem. C* **2016**, *120*, 1461−1471.
(36) Gao, R.; et al. Correlating Surface Crystal Orientation and Gas Kinetics in Perovskite Oxide Electrodes. *Adv. Mater.* **2021**, *33*, No. 2100977.
(37) Burriel, M.; et al. Influence of crystal orientation and annealing on the oxygen diffusion and surface exchange of $La_2NiO_{4+\delta}$. *J. Phys. Chem. C* **2016**, *120*, 17927−17938.
(38) Waluyo, I.; Hunt, A. Ambient Pressure X-Ray Photoelectron Spectroscopy at the IOS (23-ID-2) Beamline at the National Synchrotron Light Source II. *Synchrotron Radiat. News* **2022**, *35*, 31−38.
(39) Wang, J.; et al. Exsolution Synthesis of Nanocomposite Perovskites with Tunable Electrical and Magnetic Properties. *Adv. Funct. Mater.* **2022**, *32*, No. 2108005.
(40) Opitz, A. K.; et al. Enhancing Electrochemical Water-Splitting Kinetics by Polarization-Driven Formation of Near-Surface Iron(0): An In Situ XPS Study on Perovskite-Type Electrodes. *Angew. Chem., Int. Ed.* **2015**, *54*, 2628−2632.
(41) Kersell, H.; et al. Evolution of surface and sub-surface morphology and chemical state of exsolved Ni nanoparticles. *Faraday Discuss.* **2022**, *236*, 141−156.
(42) Berenov, A. V.; Atkinson, A.; Kilner, J. A.; Bucher, E.; Sitte, W. Oxygen tracer diffusion and surface exchange kinetics in $La_{0.6}Sr_{0.4}CoO_{3-\delta}$. *Solid State Ionics* **2010**, *181*, 819−826.
(43) Kubicek, M.; et al. Cation diffusion in $La_{0.6}Sr_{0.4}CoO_{3-\delta}$ below 800 °C and its relevance for Sr segregation. *Phys. Chem. Chem. Phys.* **2014**, *16*, 2715−2726.
(44) Jung, W.; Tuller, H. L. Investigation of Cathode Behavior of Model Thin-Film $SrTi_{1-x}Fe_xO_{3-\delta}$ (x = 0.35 and 0.5) Mixed Ionic-Electronic Conducting Electrodes. *J. Electrochem. Soc.* **2008**, *155*, B1194.
(45) Gopal, C. B.; Haile, S. M. An electrical conductivity relaxation study of oxygen transport in samarium doped ceria. *J. Mater. Chem. A* **2014**, *2*, 2405−2417.
(46) Wang, J.; et al. Strain-Dependent Surface Defect Equilibria of Mixed Ionic-Electronic Conducting Perovskites. *Chem. Mater.* **2022**, *34*, 5138−5150.
(47) Gan, Y. Atomic and subnanometer resolution in ambient conditions by atomic force microscopy. *Surf. Sci. Rep.* **2009**, *64*, 99−121.
(48) Pilling, N. B. The Oxidation of Metals at High Temperature. *J. Inst. Met.* **1923**, *29*, 529−582.
(49) Yan, L.; Balasubramaniam, K. R.; Wang, S.; Du, H.; Salvador, P. A. Effects of crystallographic orientation on the oxygen exchange rate of $La_{0.7}Sr_{0.3}MnO_3$ thin films. *Solid State Ionics* **2011**, *194*, 9−16.
(50) Schmid, A.; Rupp, G. M.; Fleig, J. How To Get Mechanistic Information from Partial Pressure-Dependent Current−Voltage Measurements of Oxygen Exchange on Mixed Conducting Electrodes. *Chem. Mater.* **2018**, *30*, 4242−4252.
(51) Cao, Y.; Gadre, M. J.; Ngo, A. T.; Adler, S. B.; Morgan, D. D. Factors controlling surface oxygen exchange in oxides. *Nat. Commun.* **2019**, *10*, 1346.

https://doi.org/10.1021/jacs.2c10256
J. Am. Chem. Soc. XXXX, XXX, XXX−XXX

(52) Heifets, E.; Goddard, W. A.; Kotomin, E. A.; Eglitis, R. I.; Borstel, G. Ab initio calculations of the $SrTiO_3$ (110) polar surface. *Phys. Rev. B* **2004**, *69*, No. 035408.
(53) Piskunov, S.; et al. Hybrid DFT calculations of the atomic and electronic structure for ABO_3 perovskite (001) surfaces. *Surf. Sci.* **2005**, *575*, 75−88.
(54) Buckner, H. B.; Perry, N. H. In Situ Optical Absorption Studies of Point Defect Kinetics and Thermodynamics in Oxide Thin Films. *Adv. Mater. Interfaces* **2019**, *6*, No. 1900496.
(55) Merkle, R.; Maier, J. Oxygen incorporation into Fe-doped $SrTiO_3$: Mechanistic interpretation of the surface reaction. *Phys. Chem. Chem. Phys.* **2002**, *4*, 4140−4148.
(56) Perry, N. H.; Kim, J. J.; Tuller, H. L. Oxygen surface exchange kinetics measurement by simultaneous optical transmission relaxation and impedance spectroscopy: $Sr(Ti,Fe)O_{3-x}$ thin film case study. *Sci. Technol. Adv. Mater.* **2018**, *19*, 130−141.
(57) Rothschild, A.; Menesklou, W.; Tuller, H. L.; Ivers-Tiffée, E. Electronic Structure, Defect Chemistry, and Transport Properties of $SrTi_{1-x}Fe_xO_{3-y}$ Solid Solutions. *Chem. Mater.* **2006**, *18*, 3651−3659.
(58) Bieger, T.; Maier, J.; Waser, R. An Optical In-Situ Method to Study Redox-Kinetics in $SrTiO_3$. *Ber. Bunsen-Ges. Phys. Chem.* **1993**, *97*, 1098−1104.
(59) De Souza, R. A.; Saiful Islam, M.; Ivers-Tiffée, E. Formation and migration of cation defects in the perovskite oxide $LaMnO_3$. *J. Mater. Chem.* **1999**, *9*, 1621−1627.
(60) Skiba, E. J.; Chen, T.; Perry, N. H. Simultaneous Electrical, Electrochemical, and Optical Relaxation Measurements of Oxygen Surface Exchange Coefficients: $Sr(Ti,Fe)O_{3-d}$ Film Crystallization Case Study. *ACS Appl. Mater. Interfaces* **2020**, *12*, 48614−48630.
(61) Crank, J.*The mathematics of diffusion*; Oxford university press, 1979.
(62) Nicollet, C.; Tuller, H. L. Perspective on the Relationship between the Acidity of Perovskite Oxides and Their Oxygen Surface Exchange Kinetics. *Chem. Mater.* **2022**, *34*, 991−997.
(63) Tsvetkov, N.; Lu, Q.; Sun, L.; Crumlin, E. J.; Yildiz, B. Improved chemical and electrochemical stability of perovskite oxides with less reducible cations at the surface. *Nat. Mater.* **2016**, *15*, 1010−1016.
(64) Nicollet, C.; et al. Acidity of surface-infiltrated binary oxides as a sensitive descriptor of oxygen exchange kinetics in mixed conducting oxides. *Nat. Catal.* **2020**, *3*, 913−920.
(65) Fairley, N.; et al. Systematic and collaborative approach to problem solving using X-ray photoelectron spectroscopy. *Appl. Surf. Sci. Adv.* **2021**, *5*, No. 100112.
(66) Nečas, D.; Klapetek, P. Gwyddion: an open-source software for SPM data analysis. *Cent. Eur. J. Phys.* **2012**, *10*, 181−188.
(67) Kalaev, D.; Tuller, H. L. Active Tuning of Optical Constants in the Visible−UV: Praseodymium-Doped Ceria—a Model Mixed Ionic−Electronic Conductor. *Adv. Opt. Mater.* **2021**, *9*, No. 2001934.
(68) Kresse, G.; Furthmüller, J. Efficient iterative schemes for ab initio total-energy calculations using a plane-wave basis set. *Phys. Rev. B* **1996**, *54*, 11169−11186.

https://doi.org/10.1021/jacs.2c10256
J. Am. Chem. Soc. XXXX, XXX, XXX−XXX